Chemical Science

Accepted Manuscript

This article can be cited before page numbers have been issued, to do this please use: Y. Yamazaki, Q. Wang, Y. Tanabe and Y. Nishibayashi, *Chem. Sci.*, 2026, DOI: 10.1039/D6SC02866G.

ROYAL SOCIETY OF CHEMISTRY

rsc.li/chemical-science

View Article Online
DOI: 10.1039/D6SC02866G

ARTICLE

Visible-Light-Driven Ruthenium-Catalyzed Hydrogenation of Manganese Nitride Complexes to Ammonia under Ambient Conditions

Received 00th January 20xx,
Accepted 00th January 20xx

DOI: 10.1039/x0xx00000x

Yasuomi Yamazaki, [a] Qiubo Wang, [a] Yoshiaki Tanabe, [a] and Yoshiaki Nishibayashi*[a]

In recent years, photocatalytic hydrogenation of metal nitrides to ammonia using solar energy as a renewable energy source and green hydrogen as both an electron and a proton source under ambient reaction conditions has been intensively investigated to achieve one of the most desirable next-generation scientific techniques, i.e., atom-economical ammonia production from dinitrogen and dihydrogen, thereby contributing to a carbon-neutral society. In this study, we have successfully developed visible-light-driven photocatalytic hydrogenation of manganese nitride complexes to ammonia at room temperature under an ambient pressure of dihydrogen in the presence of diruthenium complexes as dihydrogen oxidation catalysts and iridium complexes as photosensitizers. The turnover numbers based on the diruthenium complex and the yield of ammonia based on the manganese nitride complex reached up to 150 equiv. and 91%, respectively, indicating the high durability and efficiency of this photocatalytic system. Moreover, this hydrogenation proceeded photocatalytically even at a significantly low partial pressure of dihydrogen (down to 0.05 atm), which was much lower than in previous systems reported by other research groups, and would be a key process for paving the way for achieving the photocatalytic ammonia formation under an ambient pressure of a mixture of dinitrogen and dihydrogen.

Introduction

Ammonia is an essential nitrogen source for fertilizer and nitrogen-containing chemicals, supporting various industrial and human activities.[1] In recent years, the potential use of ammonia as a promising energy carrier and fuel for a carbon-neutral society has attracted more attention.[2-6] Currently, ammonia is industrially produced using the Haber-Bosch process from dinitrogen and dihydrogen ($N_2 + 3H_2 \rightarrow 2NH_3$). This process is one of the most desirable synthetic methods from the viewpoint of atom economy. However, the Haber-Bosch process requires high temperatures and pressures, resulting in significant energy consumption. Therefore, new environmentally friendly methods for ammonia production from dinitrogen and dihydrogen (green hydrogen in the future) that can proceed under mild reaction conditions and utilize renewable energy (typically solar energy) have been sought.

To advance in solid catalysts in the Haber-Bosch process, various photoresponsive heterogeneous photocatalysts have been widely developed to achieve solar-light-driven ammonia synthesis from dinitrogen and dihydrogen.[7-10] In addition to the heterogeneous catalysts, numerous homogeneous systems have been developed and investigated because homogeneous reaction systems are suitable for gaining molecular and mechanistic insights into the challenging goal of ammonia synthesis from dinitrogen and dihydrogen under mild reaction conditions. The first important concept in this research area was proposed in 1991, in a report on the stoichiometric protonation of a tungsten–dinitrogen complex with dihydrogen as the proton source, using the strong acidity of a ruthenium dihydrogen complex to form the corresponding tungsten hydrazido(2-) complex and ruthenium hydride complex.[11] In 1998, one of the authors of the present paper found that stoichiometric reactions between tungsten–dinitrogen complexes and an excess of ruthenium–dihydrogen complexes at 55 °C under 1 atm of dihydrogen afforded ammonia, formed via protonation of the coordinated dinitrogen with the coordinated dihydrogen.[12-14] This is one remarkable milestone as the first successful example of ammonia formation from dinitrogen and dihydrogen under mild reaction conditions. Later, Chirik and coworkers reported the hydrogenation of dinitrogen-bridged dizirconium complexes with dihydrogen to afford a stoichiometric amount of ammonia, using both electrons and protons derived from dihydrogen, as another unique and important example.[15-18] Tri(iron)bis(nitrido) complex ($[(Cp'Fe)_3(\mu_3\text{-}N)_2]$, Cp' = η^5-1,2,4-$(Me_3C)_3C_5H_2$), which was synthesized by reduction of $[Cp'Fe(\mu\text{-}I)]_2$ under dinitrogen atmosphere, is also an interesting example, because of its reactivity with dihydrogen (4 bar) at ambient temperature to form a stoichiometric amount of ammonia (3-7% yield).[19] Recently, the first example of nitrogen-nitrogen bond cleavage and subsequent hydrogenation with dihydrogen to form NH_3 using a molecular uranium complex has been reported.[20]

[a] Department of Applied Chemistry, School of Engineering, The University of Tokyo, 7-3-1 Hongo, Bunkyo-ku, Tokyo 113-8656, Japan. E-mail: ynishiba@g.ecc.u-tokyo.ac.jp

View Article Online DOI: 10.1039/D6SC02866G

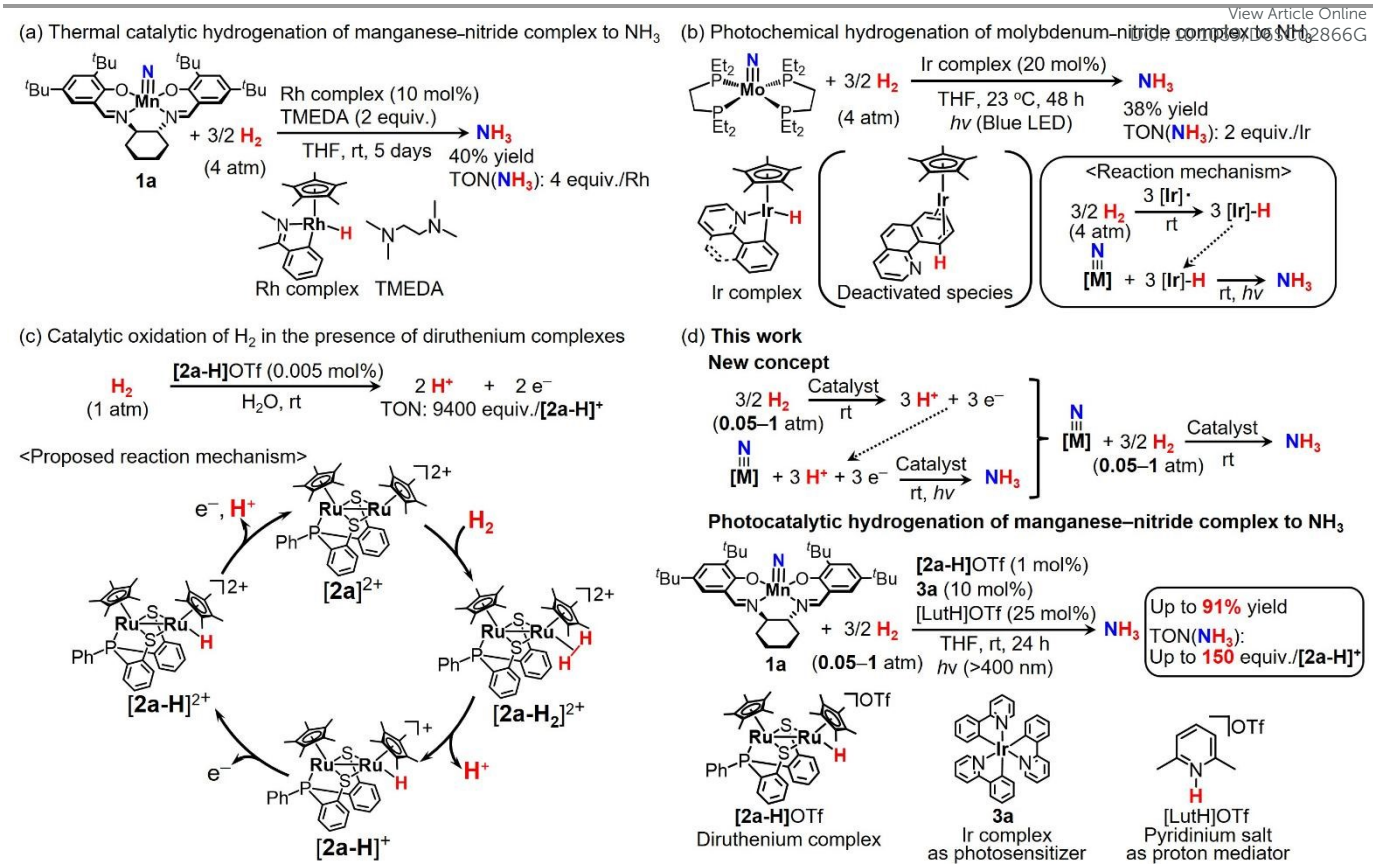

Scheme 1. (a) Thermal catalytic and (b) photocatalytic hydrogenation of metal nitride complexes under 4 atm of dihydrogen. (c) Catalytic dihydrogen oxidation using a diruthenium complex. (d) Visible-light-driven ruthenium-catalyzed hydrogenation of manganese nitride complex developed in this study.

Another useful reported strategy is the (photo)catalytic hydrogenation of transition-metal nitride complexes,[21-26] which are known to be key intermediates produced via nitrogen-nitrogen triple bond cleavage of dinitrogen in efficient catalytic nitrogen fixation.[27-43] Although, in most reported systems, dinitrogen was not used directly as a nitrogen source for nitride complexes, several (photo)catalytic systems for hydrogenation of metal nitride complexes to ammonia using dihydrogen as both an electron and a proton source have been reported over the last decade. In fact, Chirik and co-workers reported thermal catalytic hydrogenation of manganese(V) nitride complex bearing a salen ligand (**1a**) as a model metal nitride complex at room temperature under 4 atm of dihydrogen in the presence of rhodium hydride complexes to produce a stoichiometric amount of ammonia (Scheme 1a).[44] It should be noted that although **1a** cannot be produced by the activation of dinitrogen, **1a** can produce ammonia by hydrogen atom transfer (HAT)[45,46] or proton-coupled electron transfer (PCET),[47-49] as with the nitride complexes in the (photo)catalytic cycle for the ammonia formation from dinitrogen. The bond dissociation free energy of the Rh-H bond ($BDFE_{Rh-H}$) was estimated to be 51 kcal/mol, which is very close to the theoretical minimum limitation of the BDFE values towards ammonia formation because the value of $\Delta G_f°(H•)$ to split the hydrogen-hydrogen bond in dihydrogen is 52.0 kcal/mol. On the other hand, the $BDFE_{N-H}$ value of the imide complex produced by hydrogenation of **1a** was estimated to be 70 kcal/mol,[44,50] indicating that the suitable BDFE value of the Rh-H bond was effective for both hydrogen-hydrogen bond cleavage and hydrogenation of **1a**. However, likely due to the small driving force of hydrogen-hydrogen bond cleavage, the reaction rate was slow (over 5 days) to reach 40% yield at room temperature and 60% yield at 50 °C. Besides, the turnover number for ammonia production based on the Rh atom in the catalyst was not high (4-6 equiv.).

Chirik and co-workers also reported photocatalytic hydrogenation of a molybdenum nitride complex in the presence of iridium hydride complexes as photocatalysts under 4 atm of dihydrogen and visible-light irradiation to produce a stoichiometric amount of ammonia (Scheme 1b).[51] Although the BDFE value of the Ir-H bond in the ground state is approximately 60 kcal/mol, that in the excited state is estimated to be very small (approximately 10 kcal/mol), which is enough to trigger the photochemical HAT (or PCET) to the molybdenum complex ($BDFE_{N-H}$ = 21 kcal/mol). This photocatalytic HAT reaction has also been applied for the catalytic formation of weak chemical bonds in various organic compounds.[52] Notably, this molybdenum nitride complex was successfully reproduced after ammonia formation via several stepwise reactions; therefore, this reaction system is the first successful example of achieving the synthetic cycle for ammonia formation from dinitrogen and dihydrogen, though the ammonia yield based on the molybdenum nitride complex and the turnover number of ammonia formation based on the iridium complex were only 38% and 2 equiv., respectively. By changing the photocatalyst

to [Ir(ppy)$_3$]-type complex (ppy = 2-phenylpyridinato), the ammonia yield became much higher (87% under 4 atm H_2 or 75% under 1 atm H_2), and the turnover number of the molybdenum complex for ammonia formation from dinitrogen and dihydrogen reached 1.1 by repeating the synthetic cycle.[53]

One possible reason for the low turnover numbers of dihydrogen activation catalysts in the aforementioned systems is the hydrogenation of ligands, resulting in structural changes in the catalyst or ligand dissociation (e.g., photodriven C–H reductive elimination in the hydride complexes (Scheme 1b));[44,54] therefore, the use of stable catalysts for dihydrogen activation should be necessary to achieve durable catalytic systems. Our group previously reported highly durable and efficient catalytic oxidation of dihydrogen under ambient reaction conditions using thiolate-bridged diruthenium complexes (Scheme 1c).[55-57] In this reaction, monocationic hydride complex (**[2a-H]**$^+$), which is produced by the coordination of dihydrogen to dicationic complex (**[2a]**$^{2+}$) with a vacant site and subsequent deprotonation, provides an electron, a proton, and an electron in that order to reproduce **[2a]**$^{2+}$. As a result, dihydrogen can be used as both a two-electron and a two-proton donor to reduce oxidants (e.g., ferrocenium salts) and protonate bases (e.g., pyridine derivatives), respectively. Notably, the maximum turnover number for the reduction of ferrocenium cation exceeded 9400 equiv. based on **[2a-H]**$^+$. Moreover, this dihydrogen oxidation with **[2a-H]**OTf proceeded efficiently even under 0.37 atm of dihydrogen, suggesting that **[2a-H]**OTf can supply electrons and protons derived from dihydrogen with high durability and efficiency even under low partial pressure of dihydrogen.

Based on these research backdrops, we have envisaged a new concept that uses our unique dihydrogen activation method to catalytically reduce metal nitride complexes to ammonia (Scheme 1d). In this concept, two electrons and two protons derived from dihydrogen are transferred separately to **1a** by a photosensitizer and a proton mediator, respectively, unlike the reported systems with hydride complexes in Schemes 1a and 1b. In fact, we have succeeded in developing photocatalytic hydrogenation of the manganese nitride complex **1a** as a typical model metal nitride complex in the presence of the diruthenium complex **[2a-H]**OTf as a dihydrogen oxidation catalyst. Since the reducing power of **[2a-H]**OTf is not enough to donate electrons directly to **1a** (or its derivatives), we have newly designed a combination system consisting of a catalytic cycle for oxidizing dihydrogen with **[2a-H]**OTf to provide electrons and protons and a photosensitizing cycle with Ir(ppy)$_3$ (**3a**) as a redox photosensitizer to increase the electron-donating ability and trigger hydrogenation of **1a** using electrons and protons derived from dihydrogen via photochemical PCET or HAT processes under ambient reaction conditions and visible light irradiation, resulting in up to 150 equivalents of the turnover number for ammonia formation based on **[2a-H]**OTf and 91% of the ammonia yield based on **1a**. Moreover, this hydrogenation proceeded photocatalytically even under 0.05 atm of dihydrogen, demonstrating a useful feature for achieving photocatalytic ammonia formation under ambient pressure of a mixture of dinitrogen and dihydrogen.

Results and discussion

View Article Online
DOI: 10.1039/D6SC02866G

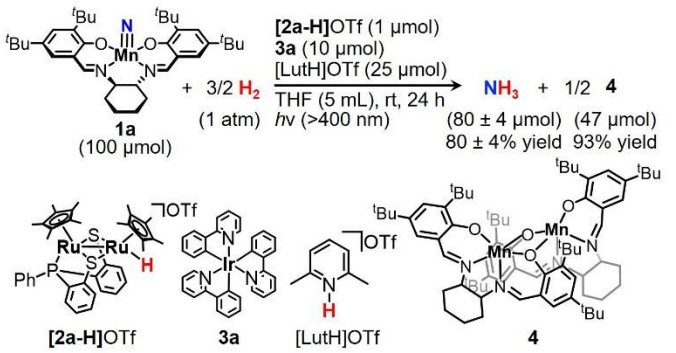

Figure 1. Photo-driven ruthenium-catalyzed hydrogenation of manganese nitride complex.

As a typical run, we performed the photocatalytic hydrogenation of the manganese nitride complex **1a** as a model metal nitride complex (100 μmol) in the presence of catalytic amounts of the diruthenium complex **[2a-H]**OTf (1 μmol) as a dihydrogen oxidation catalyst, the iridium complex **3a** (10 μmol) as a photosensitizer, and 2,6-lutidinium triflate ([LutH]OTf, 25 μmol) as a proton mediator in tetrahydrofuran (THF, 5 mL) under visible light irradiation (>400 nm) and 1 atm of dihydrogen at room temperature for 24 h (Figure 1; Table 2, entry 1). After photoirradiation, the solution color changed from green to orange (Figure S2 in the Supporting Information). The amount of produced ammonia reached 80 ± 4 μmol (i.e., 80 equiv. based on **[2a-H]**OTf in 80% yield based on **1a**). To obtain 80 μmol of ammonia, 240 μmol (= 80 × 3 μmol) of protons and electrons are required; hence, the turnover number of the proton mediator and the photosensitizer was larger than 9 and 24, respectively. Figure 2a illustrates the time course of the amount of ammonia produced in the photocatalysis. During the reaction, the reaction rate of ammonia formation gradually decreased and reached a plateau in 24 h of irradiation (Figure 2a, Table S1 in the Supporting Information). A light-on/off experiment under the same reaction conditions revealed that ammonia formation proceeded only during photoirradiation, and a radical chain reaction should not have proceeded in this reaction system (Figure 2b, Table S6 in the Supporting Information). The use of ^{15}N-labeled manganese nitride complex (**^{15}N-1a**) under the same reaction conditions afforded ^{15}N-labeled ammonia ($^{15}NH_3$) in 76% yield, confirming that ammonia was produced from hydrogenation of the nitride moiety of **1a** (Figure S3 in the Supporting Information). The apparent quantum yield of the ammonia formation (Φ_{NH3}) in the initial stage of the photoreaction was estimated to be 0.86% using a 405-nm monochromatic light and a ferrioxalate chemical actinometer[58] (Table S8 in the Supporting Information). The relatively low quantum yield is mainly due to the strong inner-filter effect[59] by **1a** and unexpected charge recombination pathways (*vide infra*). The photocatalysis under D_2 for 12 h (18% yield, Table S7 in the Supporting Information) exhibited a much lower reaction rate than under H_2 (54% yield). The kinetic isotope effect (KIE) was estimated to be 3.1,

suggesting that proton or hydrogen-atom transfer and/or reaction with dihydrogen should be included among the rate-determining steps (see below).

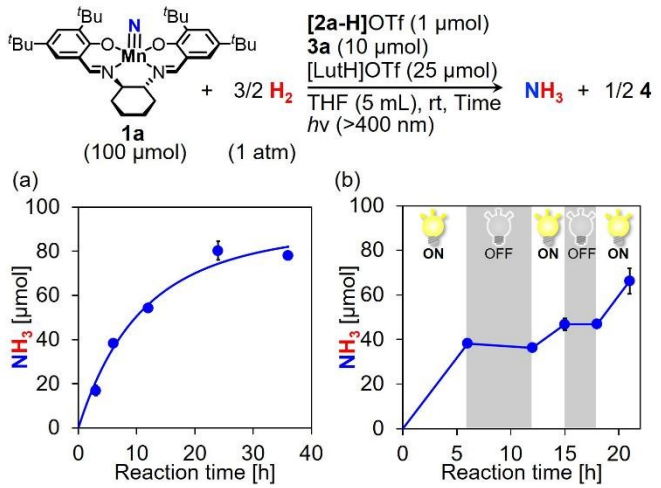

Figure 2. (a) The time course of the amount of ammonia produced in the photocatalysis. (b) The light on/off experiment.

Table 1. Results of control experiments.

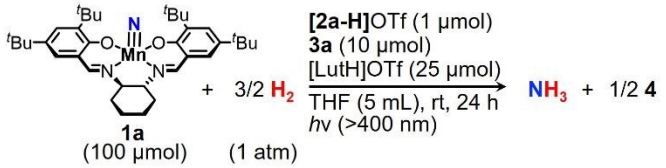

Entry	Deviations from standard conditions	NH_3 yield [%][a,b]
1	—	80 ± 4
2	Without **1a**	<1
3	Without **[2a-H]**OTf	5 ± 1
4	Without **3a**	1 ± 1
5	Without [LutH]OTf	21 ± 1
6	Without light	3 ± 1
7	Without H_2 (Under Ar)	7 ± 1

[a] The averages are shown with standard errors. [b] Yield based on **1a**.

Several control experiments shown in Table 1 confirmed that the combination of **1a**, **[2a-H]**OTf, **3a**, [LutH]OTf, dihydrogen, and visible light was required for the efficient ammonia formation. It should be noted that the photocatalytic hydrogenation proceeded slowly even in the absence of [LutH]OTf as a proton mediator (Entry 5 in Table 1), likely because protons were directly donated from the diruthenium complex to **1a** in the PCET process due to the high acidity of the intermediates (see below). On the other hand, in the case without **[2a-H]**OTf (Entry 3 in Table 1), the amount of ammonia was low, though protons can be provided by [LutH]OTf (i.e., 25 μmol of protons). This result clearly demonstrates that, under the conditions of the control experiment, the sole electron source was **3a** (i.e., 10 μmol of **3a** can produce at most 3.3 μmol of ammonia), whereas under standard conditions, electrons were catalytically supplied via the dihydrogen oxidation reaction with **[2a-H]**OTf.

The detailed structure of the resulting manganese complex after hydrogenation of **1a** has not yet been reported; therefore, we isolated the manganese complex by removing the solvent from the reaction solution under reduced pressure, extracting it from the obtained residue with hexane, and then filtering off the insoluble materials including catalysts and [LutH]OTf (yield: 93%, see section 2.7 in the Supporting Information). Single crystals were successfully prepared by slow evaporation of the hexane solution, and the X-ray analysis revealed that the product was the dinuclear manganese complex (**4**) bridged by one of the oxygen atoms in each salen ligand (Figure 3a, Table S10 in the Supporting Information). The elemental analysis also confirmed the composition formula of **4** and the purity of the sample. The manganese nitride complex **1a** was regenerated from **4** using the synthetic method reported by Chirik *et al.* in a moderate yield (Figure 3b, Figures S7 and S8 in the Supporting Information); therefore, **4** should be the same as or similar to the manganese species obtained after the photoreactions in the aforementioned reported systems.[44,50,60] However, **4** exhibited no signal in the electron spin resonance (ESR) spectrum (Figure S9 in the Supporting Information), in contrast to the aforementioned reported systems, which showed a strong isotropic signal with the g value of 2.0.[44] ^{1}H NMR spectrum of **4** also indicated its weak magnetism because of the relatively small difference in chemical shifts from those of diamagnetic complex **1a** (Figure S4 in the Supporting Information). These results suggest that **4** can be assigned as a homovalent antiferromagnetically coupled dimer.[61,62] Quite interestingly, we found that the ESR spectrum of the solution containing **4** and [LutH]OTf (Figures S9 in the Supporting Information) contained a characteristic signal containing 6 lines, which is a typical signal shape for Mn^{II} species because of the interaction between the $3d^5$ electronic spin (S = 5/2) with the nuclear spin of the ^{55}Mn nucleus (I = 5/2)[63]. The UV-vis absorption spectrum of **4** was also changed drastically by adding [LutH]OTf (Figure S10 in the Supporting Information). In the case of the solution after the photoreaction shown in Figure 1, quite weak but similar signals were also observed in the ESR spectrum, while its UV-vis absorption spectrum was well simulated with the spectrum of **4**, meaning that **4** in the reaction solution had slightly reacted with [LutH]OTf (Figures S5 in the Supporting Information). Given that the addition of Lut did not affect both ESR and UV-vis absorption spectra (Figures S9 and S10 in the Supporting Information), protonation of **4** with [LutH]OTf to form monomeric Mn^{II} species might be involved in the structural changes, even though the resulting molecular structure is unclear at this stage. The simulation spectra and further discussion on the spectrum structure are included in section 2.10 of the Supporting Information.

View Article Online
DOI: 10.1039/D6SC02866G

Table 2. Photocatalytic hydrogenation of manganese nitride complexes under 1 atm of H_2 in the presence of catalysts, photosensitizers, and proton mediators.

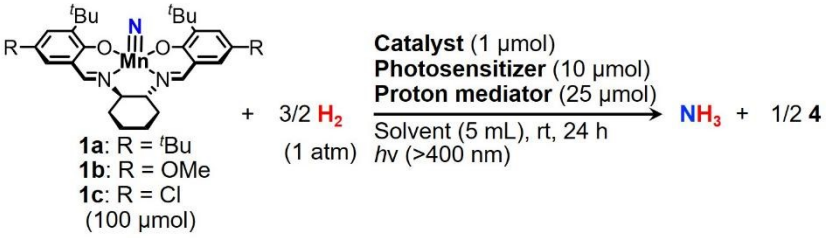

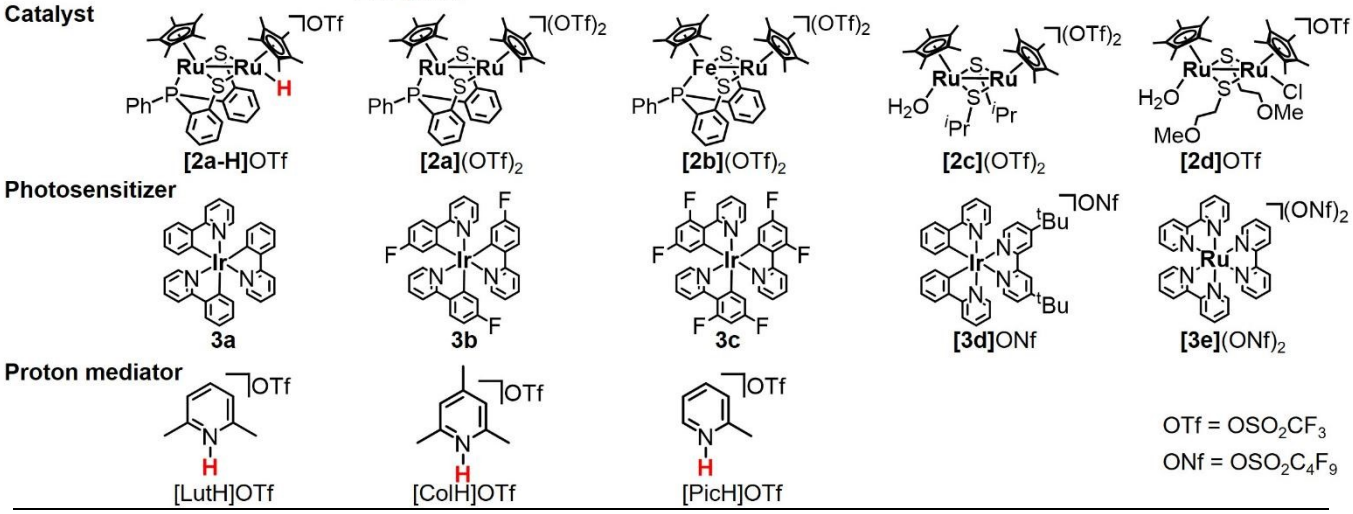

Entry	Nitride complex	Catalyst	Photosensitizer	Proton mediator	Solvent	NH_3 production [μmol]	NH_3 yield [%]
1	**1a**	**[2a-H]**OTf	**3a**	[LutH]OTf	THF	80 ± 4	80 ± 4
2[a]	**1a**	**[2a-H]**OTf	**3a**	[LutH]OTf	THF	110 ± 3	55 ± 2
3[b]	**1a**	**[2a-H]**OTf	**3a**	[LutH]OTf	THF	150 ± 4	75 ± 2
4	**1a**	**[2a]**$(OTf)_2$	**3a**	[LutH]OTf	THF	83 ± 2	83 ± 2
5	**1a**	**[2b]**$(OTf)_2$	**3a**	[LutH]OTf	THF	33 ± 2	33 ± 2
6	**1a**	**[2c]**$(OTf)_2$	**3a**	[LutH]OTf	THF	14 ± 1	14 ± 1
7	**1a**	**[2d]**OTf	**3a**	[LutH]OTf	THF	8 ± 0.5	8 ± 0.5
8[c]	**1a**	**[2a-H]**OTf	**3a**	[LutH]OTf	THF	81 ± 2	81 ± 2
9[d]	**1a**	**[2a-H]**OTf	**3a**	[LutH]OTf	THF	46 ± 5	46 ± 5
10	**1a**	**[2a-H]**OTf	**3b**	[LutH]OTf	THF	56 ± 5	56 ± 5
11	**1a**	**[2a-H]**OTf	**3c**	[LutH]OTf	THF	14 ± 1	14 ± 1
12	**1a**	**[2a-H]**OTf	**[3d]**ONf	[LutH]OTf	THF	24 ± 5	24 ± 5
13	**1a**	**[2a-H]**OTf	**[3e]**$(ONf)_2$	[LutH]OTf	THF	1 ± 0.1	1 ± 0.1
14	**1a**	**[2a-H]**OTf	**3a**	[ColH]OTf	THF	69 ± 4	69 ± 4
15	**1a**	**[2a-H]**OTf	**3a**	[PicH]OTf	THF	65 ± 2	65 ± 2
16[e]	**1a**	**[2a-H]**OTf	**3a**	[LutH]OTf	THF	64 ± 1	64 ± 1
17[f]	**1a**	**[2a-H]**OTf	**3a**	[LutH]OTf	THF	52 ± 1	52 ± 1
18[g]	**1a**	**[2a-H]**OTf	**3a**	–	THF	21 ± 0.2	21 ± 0.2
19	**1a**	**[2a-H]**OTf	**3a**	[LutH]OTf	Benzene	20	20
20	**1a**	**[2a-H]**OTf	**3a**	[LutH]OTf	CH_2Cl_2	19	19
21	**1a**	**[2a-H]**OTf	**3a**	[LutH]OTf	Et_2O	6	6
22	**1b**	**[2a-H]**OTf	**3a**	[LutH]OTf	THF	58 ± 2	58 ± 2
23	**1c**	**[2a-H]**OTf	**3a**	[LutH]OTf	THF	10 ± 1	10 ± 1

[a] **1a** (200 μmol) was used. [b] The amount of **1a** and [LutH]OTf were changed to 200 and 50 μmol, respectively. [c] **[2a-H]**OTf (2 μmol) was used. [d] **[2a-H]**OTf (0.5 μmol) was used. [e] [LutH]OTf (50 μmol) was used. [f] [LutH]OTf (10 μmol) was used. [g] [LutH]OTf was not used.

View Article Online DOI: 10.1039/D5SC02866C

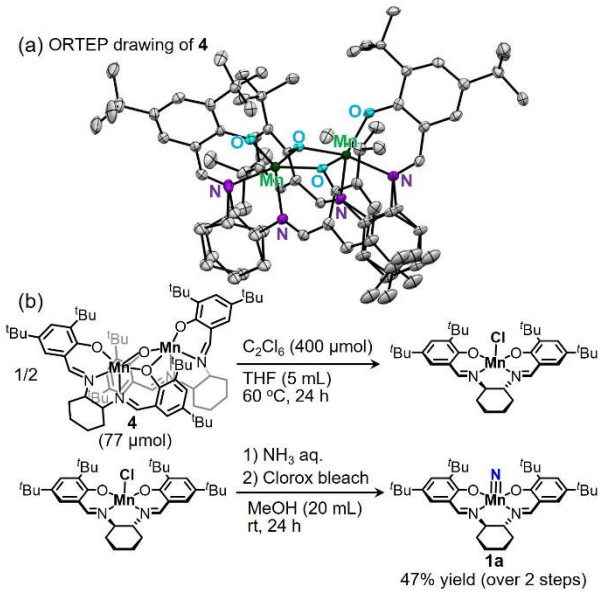

Figure 3. (a) An ORTEP drawing of the resulting dimanganese complex **4** obtained after the photocatalytic hydrogenation. Thermal ellipsoids are shown at the 50% level. Hydrogen atoms and solvent molecules are omitted for clarity, and the main places in the disordered regions are illustrated. White, blue, purple, and green correspond to C, O, N, and Mn atoms, respectively. (b) Reproduction of **1a** from **4**.

The residue obtained after extracting **4**, as described above, was further investigated. In the ^{1}H NMR spectrum of the residue, **[2a-H]**(OTf) (1.0 μmol) and **3a** (10 μmol) were observed, meaning that the decomposition of the catalysts was not significant even after the 24-hour reaction (Figure S6 in the Supporting Information). Therefore, we increased the amount of **1a** from 100 to 200 μmol. It is noted that this concentration of **1a** is almost at saturation. The amount of produced ammonia was increased to 110 μmol, while the yield was decreased to 55% (Table 2, entry 2). When simultaneously increasing the amount of [LutH]OTf to 50 μmol, the amount and yield of produced ammonia were further increased to 150 μmol and 75%, respectively (Table 2, entry 3). This is probably because of the high concentration of the oxidation product **4** and the aforementioned interaction between [LutH]OTf and **4**, which led to the suppression of the function of [LutH]$^+$ as a proton mediator.

Next, to optimize the reaction conditions, we conducted the photocatalytic hydrogenation of **1a** using various catalysts for dihydrogen oxidation (Table 2; entries 1, 4-7). The time courses of the amount of ammonia produced during the photocatalytic reactions are summarized in Figure 4 and Tables S1-5 in the Supporting Information. When using the corresponding dicationic complex **[2a]**$(OTf)_2$, which possesses a vacant site, both the reaction rate and the amount of produced ammonia became almost the same as those using **[2a-H]**(OTf). This result clearly indicates that **[2a-H]**(OTf) and **[2a]**$(OTf)_2$ were efficiently and mutually converted in the catalytic cycle, as with the aforementioned system. A Ru-Fe dinuclear complex (**[2b]**$(OTf)_2$) also functioned as an effective catalyst in the initial stage, even though the reaction ceased within 6 h of irradiation, likely because of the lower durability of the Fe unit. In the photocatalytic reactions using **[2c]**$(OTf)_2$ or **[2d]**OTf, which possess two thiolate ligands, both the reaction rate in the initial stages and the amount of produced ammonia became much lower than those using **[2a-H]**(OTf). From these results, the multidentate thiolate ligand, including the triaryl phosphine moiety, is suitable for improving catalyst durability. Further discussion with cyclic voltammetry and photophysical properties is included in sections 4 and 5 of the Supporting Information. The increase in the amount of **[2a-H]**(OTf) (2 μmol) used hardly affected the photocatalytic activity (81% yield, Table 2, entry 8), while the decrease in the amount of **[2a-H]**(OTf) (0.5 μmol) used lowered the photocatalytic activity (46% yield, Table 2, entry 9), meaning that under the optimized conditions, the catalytic cycle with **[2a-H]**(OTf) may not be included in the rate-determining steps and 1 μmol or larger amount of **[2a-H]**(OTf) is required for the efficient reaction procedures (Figure S11a in the Supporting Information).

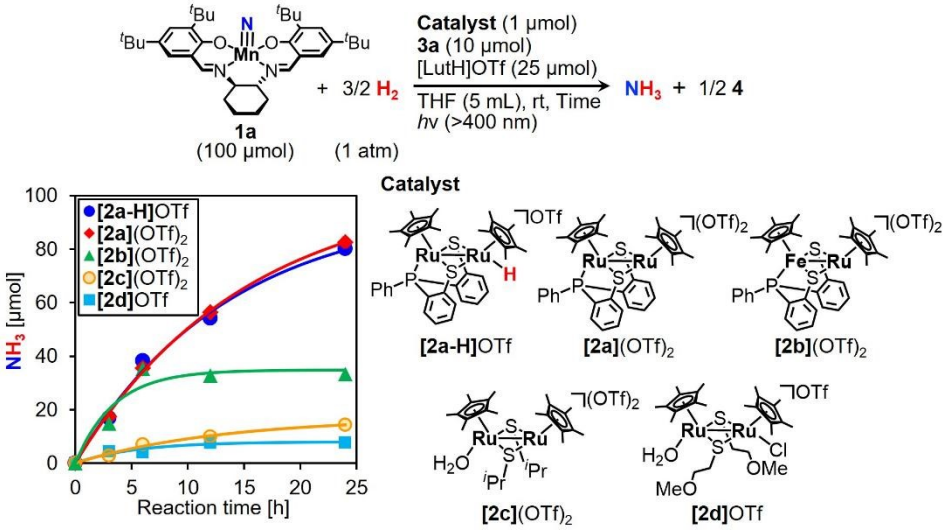

Figure 4. The time courses of the amount of ammonia produced in the photocatalysis using various thiolate-bridged dinuclear complexes (**[2a-H]**OTf (blue circle), **[2a]**$(OTf)_2$ (red diamond), **[2b]**$(OTf)_2$ (green triangle), **[2c]**$(OTf)_2$ (orange circle), **[2d]**OTf (sky blue square)).

The substituent effect on the iridium photosensitizer was also significant. When introducing electron-withdrawing fluorine groups (i.e., **3b** and **3c**), the catalytic activity decreased compared with **3a** (Table 2; entries 1, 10, 11). These results suggest that high reducing power is crucial for effective electron transfer to manganese nitride complexes (or proton mediators), thereby achieving high catalytic activity. Of note, their reducing power in the excited state (oxidation potential in the excited state (E_{ox}*)) was estimated by oxidation potentials determined by cyclic voltammetry and excitation energies determined by Franck-Condon analysis[64] as mentioned below (E_{ox}*(**3a**): −2.15 V, E_{ox}*(**3b**): −2.05 V, E_{ox}*(**3c**): −1.91 V, Table S16 in the Supporting Information). On the other hand, **[3d]**ONf (E_{ox}*: −1.39 V) and **[3e]**$(ONf)_2$ (E_{ox}*: −1.14 V), whose reducing power in the excited states is relatively weak, did not function as effective photosensitizers (Table 2; entries 12 and 13). In the case using **[3d]**ONf or **[3e]**$(ONf)_2$, according to their redox potentials, they possibly donate electrons to **1a** via reductive quenching, which is an electron transfer from **[2a-H]**OTf (E_{ox}: +0.24 V) to the excited state of a photosensitizer, due to the relatively high oxidizing power in their excited state (E_{red}*([**3b**]ONf): +0.34 V, E_{red}*([**3e**]$(ONf)_2$): +0.21 V) (Table S16 in the Supporting Information). However, their high oxidizing power might trigger the oxidation of **1a** (E_{ox}: +0.26 V) as a side reaction, thereby suppressing both the reduction of **1a** and the photosensitizing reaction by charge recombination. Consequently, these screening results suggest that using a photosensitizer with relatively low photo-oxidizing power to prevent the unexpected oxidation of **1a** and high reducing power to provide electrons to **1a** could be key to achieving high catalytic activity. All of the electrochemical and photophysical properties of the photosensitizers are summarized in Figure S28 and Table S16 of the Supporting Information.

Not only the catalysts and photosensitizers but also proton mediators, reaction solvents, and the ligand of the manganese nitride complex were optimized. The photocatalytic reaction using [LutH]OTf (80% yield) showed the highest photocatalytic activity, but [ColH]OTf (69% yield) and [PicH]OTf (65% yield) also functioned as effective proton mediators (Table 2; entries 1, 14, 15). The cyclic voltammetry suggested that all of these proton mediators (E_{red}([LutH]OTf): −1.91 V, E_{red}([ColH]OTf): −2.08 V, E_{red}([PicH]OTf): −1.85 V) can accept electrons exergonically from the excited state of **3a** (**3a***, E_{ox}*: −2.15 V) (*vide infra*). The electrochemical properties of the proton mediators are summarized in sections 4 and 5 of the Supporting Information. Although the photocatalytic reaction slowly proceeded even in the absence of [LutH]OTf (21% yield), the increase in the amount of [LutH]OTf to 10 μmol (52% yield) or 25 μmol (80% yield) led to higher photocatalytic activities (Table 2; entries 1, 17-18). The use of an even higher amount of [LutH]OTf (50 μmol) led to a similar yield to that with 25 μmol (64% yield, Table 2; entry 16). These results clearly suggest that the proton transfer from the diruthenium complexes to manganese nitride complexes was largely promoted by the pyridinium salts as proton mediators (*vide infra*).

When changing the solvent from THF (80% yield) to benzene (20% yield), CH_2Cl_2 (19% yield), or Et_2O (6% yield), the photocatalytic activities decreased drastically (Table 2; entries 1, 19-21), meaning that THF is a suitable solvent for this system. It is noted that, especially when using benzene and Et_2O, the solubility of **3a** was low, resulting in low photosensitizer concentrations and decreased photocatalytic activity (Figure S2d in the Supporting Information). The low solubility of **1a** in Et_2O might also reduce the efficiency of the photosensitizing process due to its low solution concentration and light scattering.

The effect of substituents on the salen ligand of the manganese nitride complexes also affected the catalytic activity. When introducing MeO groups (**1b**) or Cl groups (**1c**) instead of ^{t}Bu groups on the phenyl rings in the salen ligand, the yields of ammonia became 58% and 10%, respectively (Table 2, entries 22 and 23). One of the main reasons for lower yields when using **1b** or **1c** is their lower solubility, which leads to suspension and light scattering (Figure S2d in the Supporting Information). The electrochemical studies revealed that the electron-accepting abilities of **1b** (E_{red}: −2.55 V) and **1c** (E_{red}: −2.30 V) were similar to or higher than that of **1a** (E_{red}: −2.60 V), indicating that the enhancement of electron-accepting ability by changing the substituents on the salen ligand did not effectively improve the catalytic activity. In the case using **1b**, the red shift of the absorption band might have increased the inner-filter effect,[59] which suppresses the absorption of the irradiated photons by **3a** (Figure S14 in the Supporting Information), thereby reducing the efficiency of the photoreaction (*vide infra*). All of the electrochemical and photophysical properties of the manganese complexes are summarized in sections 4 and 5 of the Supporting Information.

Table 3. Photocatalytic hydrogenation of manganese nitride complexes under various partial pressures of H_2 in the presence of **[2a-H]**OTf, **3a**, and [LutH]OTf.[a]

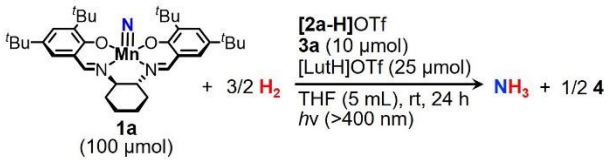

Entry	H_2 pressure [atm]	Amount of **[2a-H]OTf** [μmol]	NH_3 yield [%]
1	1	1	80 ± 4
2	0.2	1	37 ± 2
3	0.2	8	91 ± 2
4	0.05	1	19 ± 2
5	0.05	8	39 ± 1

[a] Photocatalytic reactions were performed under a mixture of H_2 (X [atm]) and N_2 (1-X [atm]). The summation pressure was 1 atm.

As described above, the manganese nitride complex was successfully hydrogenated to produce ammonia photocatalytically under 1 atm of dihydrogen as both an electron and a proton source at room temperature by using a combination of **[2a-H]**(OTf), **3a**, and [LutH]OTf. We next conducted the photocatalytic hydrogenation under a lower partial pressure of dihydrogen (Table 3, Table S9 in the

Supporting Information). The photocatalytic hydrogenation of **1a** proceeded even under 0.2 and 0.05 atm, and the yields of ammonia were 37% and 19%, respectively (Table 3, entries 2 and 4). The reaction rates linearly depended on the partial pressure of dihydrogen (Figure S11b in the Supporting Information). When increasing the amount of **[2a-H]**(OTf) from 1 μmol to 8 μmol, the amount of ammonia produced under 0.2 and 0.05 atm of dihydrogen also increased to 91% and 39%, respectively (Table 3, entries 3 and 5). These results indicate that under 0.2 or 0.05 atm of dihydrogen, the rate-determining step might have switched to the catalytic cycle for dihydrogen oxidation with **[2a-H]**OTf. It should be noted that the partial pressure of dihydrogen in the aforementioned system is much lower than that in the reported photocatalytic systems (1-4 atm)[44,51,53]. Therefore, the photocatalytic system developed in this study can effectively utilize much lower concentrations of dihydrogen.

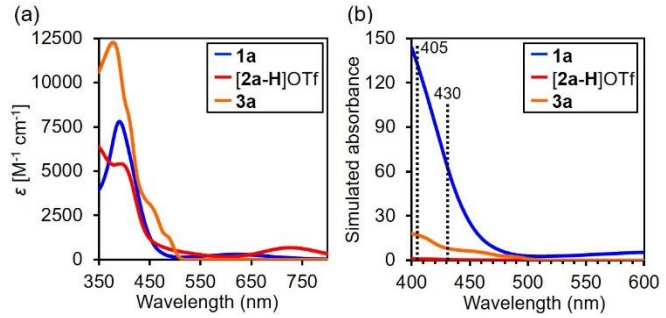

Figure 5. (a) UV-vis absorption spectrum of **1a** (blue), **[2a-H]**OTf (red), and **3a** (orange) in THF. The spectrum simulated using molar extinction coefficients and concentrations in reaction solutions for photocatalytic reactions is illustrated in (b). The concentrations of **1a**, **[2a-H]**OTf, and **3a** are 20, 0.2, and 2 mM, respectively.

To gain insight into the reaction mechanism of this photocatalytic system under the optimized reaction conditions, we investigated the photophysical and photochemical properties of the catalysts and substrates. Figure 5a illustrates the UV-vis absorption spectra of **1a**, **[2a-H]**OTf, and **3a** in THF. Photosensitizer **3a** showed absorption bands up to approximately 500 nm. Notably, **1a** and **[2a-H]**OTf showed strong absorption bands in a similar region; therefore, the absorption of the irradiation light by **3a** will be suppressed by the inner filter effect derived from **1a** and **[2a-H]**OTf. [LutH]OTf did not show any absorption bands in the visible regions. Figure 5b illustrates the absorption spectrum simulated using the molar extinction coefficients (ε) shown in Figure 5a and the concentrations in the reaction solutions under the optimized conditions, clearly demonstrating that due to the quite high concentration of **1a**, the photons irradiated to the reaction solutions were absorbed mainly by **1a**. The main irradiation wavelengths absorbed by **3a** were 405 and 430 nm, and the ratios of the photons with these wavelengths absorbed by **3a** were estimated to be only 11%. These low absorption ratios should be one of the reasons for the low quantum efficiency of the photocatalytic reactions. It is noteworthy that the dimanganese complex **4**, which is a product of the photocatalytic hydrogenation of **1a**, also exhibited relatively strong visible-light absorption ability (Figure S14b in the Supporting Information), meaning that the inner filter effect derived from **4** is also considerable.

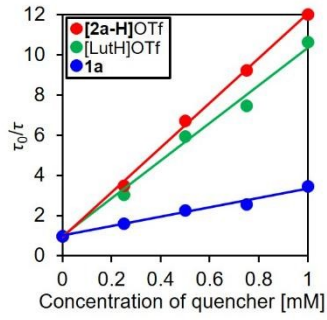

Figure 6. Stern-Volmer luminescence quenching studies of **3a** with **1a** (blue), **[2a-H]**OTf (red), or [LutH]OTf (green).

Table 4. Quenching experiments with **3a** in the presence of **1a**, **[2a-H]**OTf, or [LutH]OTf.

Quencher	K_{SV} [mM^{-1}]^a	k_Q [M^{-1} s^{-1}]^b	η_q [%]^c
1a	2.4	1.6×10^9	49
[2a-H]OTf	11	7.6×10^9	2
[LutH]OTf	9.3	6.4×10^9	48

^{a} The Stern-Volmer constants determined from the slope of the fitting curves illustrated in Figure 6. ^{b} The quenching rate constants determined from K_{SV} and the emission lifetime of **3a** in the absence of any quencher (τ_0, $K_{SV} = k_Q\tau_0$). ^{c} The quenching fractions in the reaction solution calculated based on eqn. S7 in the Supporting Information.

To investigate the behavior after the photoexcitation, the photochemical properties of **3a** were investigated using luminescence quenching experiments, i.e., Stern-Volmer analyses (Figure 6, Table 4; Figure S20 and Table S12 in the Supporting Information). It should be noted that the Stern-Volmer analyses were conducted using the emission lifetimes in the presence of quenchers (τ) and in the absence of them (τ_0) because **1a** and **[2a-H]**OTf showed strong absorption bands in the visible regions (Figure 5a) to absorb the photoluminescence from **3a** in the excited state (**3a***) resulting in the overestimation of the degree of photoluminescence quenching determined from emission intensities. The photoluminescence from **3a*** was effectively quenched by **1a**, **[2a-H]**OTf, or [LutH]OTf, and the Stern-Volmer constants (K_{SV}s) were respectively determined to be 2.4, 11, and 9.3 [mM^{-1}] from the slopes of the fitting curves of Stern-Volmer plots in Figure 6. The quenching rate constants (k_Q) calculated from the K_{SV} values and τ_0 were 1.6×10^9, 7.6×10^9, and 6.4×10^9 [$M^{-1}s^{-1}$], respectively. These values are close to the diffusion rate constants ($\approx10^{10}$ [$M^{-1}s^{-1}$]), indicating relatively high quenching efficiency. Given the K_{SV} values and their concentrations under the optimized reaction conditions, the quenching fractions (η_q) with **1a**, **[2a-H]**OTf, or [LutH]OTf were estimated to be 49%, 2%, and 48%, respectively. These results indicate that the excited state of **3a** is mainly quenched by **1a** or [LutH]OTf (see section 4.3 in the Supporting Information).

View Article Online
DOI: 10.1039/D5SC02866G

Table 5. Redox potentials of **1a**, **[2a-H]**OTf, **[2a]**$(OTf)_2$, **3a**, and [LutH]OTf.[a]

Compound	E_{red} [V]	E_{ox} [V]	E_{red}* [V][b]	E_{ox}* [V][b]
1a	−2.60[c]	+0.26	–	–
[2a-H]OTf	−1.58 −2.24	+0.24[c]	–	–
[2a](OTf)$_2$	−0.66 −1.22	–	–	–
3a	−2.84	+0.27	−0.42	−2.15
[LutH]OTf	−1.91[c]	–	–	–

[a] Measured by cyclic voltammetry under a N_2 atmosphere in THF containing 0.1 M of $^nBu_4NPF_6$ as a supporting electrolyte. The scan rate was 100 mV/s. Potentials are indicated vs. $Fc^{0/+}$. [b] The redox potentials in the excited states. [c] Peak potentials.

To consider the reasons for the photoluminescence quenching, we next measured cyclic voltammograms of the catalysts and substrates to investigate the possibility of the photo-induced electron transfer (Figures S22-29 in the Supporting Information). The redox potentials of the catalysts and substrates used under the optimized conditions are summarized in Table 5. The reduction (E_{red}) and oxidation potential (E_{ox}) of **3a** were −2.84 and +0.27 V vs. $Fc^{0/+}$, respectively. The excited energy ($E_{0\text{-}0}$) was estimated to be 2.42 eV from Franck-Condon analysis (Figure S18 in the Supporting Information); the reduction and oxidation potentials in the excited states (E_{red}* and E_{ox}*) were determined to be −0.42 V and −2.15 V, respectively. Given the oxidation potential of **1a** (E_{ox}: +0.26 V) and **[2a-H]**OTf (E_{ox}: +0.24 V), the electron transfer from **1a** or **[2a-H]**OTf to **3a*** (i.e., reductive quenching of **3a*** by **1a** or **[2a-H]**OTf) should not be the main pathway for the photoluminescence quenching. On the other hand, the oxidation potential of **3a** in the excited states was highly negative (E_{ox}*: −2.15 V) enough to exergonically trigger oxidative quenching, i.e., electron transfer to **[2a-H]**OTf (E_{red}: −1.58 V) or [LutH]OTf (E_{red}: −1.91 V). It is noteworthy that **[2a]**$(OTf)_2$, which is an important intermediate of the hydrogen oxidation cycle with **[2a-H]**OTf, showed more positive reduction potentials (E_{red}: −0.66, −1.22 V), meaning that oxidative quenching by **[2a]**$(OTf)_2$ will also proceed efficiently. The reduction of **[2a-H]**OTf and **[2a]**$(OTf)_2$ will suppress the oxidation of dihydrogen to decrease the efficiency of the photocatalytic reactions, though the quenching efficiency with **[2a-H]**OTf or **[2a]**$(OTf)_2$ is not high due to their low concentrations. The oxidative quenching by [LutH]OTf will produce LutH$^\bullet$ radical species, which potentially function as hydrogen-atom donors;[45,46] therefore, this quenching process should be one of the main pathways for the hydrogenation of **1a** (see below). The reduction potential of **1a** (E_{red}: −2.60 V) is more negative than E_{ox}* of **3a** (E_{ox}*: −2.15 V), indicating that direct single-electron transfer will not proceed efficiently; therefore, proton-coupled electron transfer from **3a*** with $[LutH]^+$ to **1a**, rather than the single-electron transfer, should be a plausible pathway. Notably, as illustrated in Figure 5, **1a** exhibits strong absorption over a wide range of the visible region, and the emission spectrum of **3a** and the absorption spectrum of **1a** overlap significantly (Figure S19 in the Supporting Information); therefore, excitation energy transfer from **3a*** to **1a** should also be considered. This excitation energy transfer lowers the concentration of **3a***, thereby reducing the efficiency of photosensitizing reactions. Consequently, the photoluminescence quenching by **1a** includes both photo-induced electron transfer and/or PCET from **3a*** to **1a** and the excitation energy transfer, and the former process is the other main pathway for the hydrogenation of **1a** (*vide infra*).

The PCET with **3a*** and [LutH]OTf to **1a** is a thermodynamically favorable process since the effective BDFE value of the combination of **3a*** and $[LutH]^+$ (23 kcal/mol, see section 5.3 in the Supporting Information) is much smaller than the $BDFE_{N\text{-}H}$ value of the manganese-imide complex corresponding to **1a** (70 kcal/mol, Figure 7a).[50] However, photo-induced PCET within its short excitation lifetimes (< 1.6 μs) might be difficult to occur, as the three molecules need to approach simultaneously. In general, an interaction between two of them, e.g., hydrogen bond formation, can promote PCET among three molecules. Therefore, to investigate the possibility of the photo-induced PCET, we measured ^{15}N NMR of THF solution containing **^{15}N-1a** (0.04 M) and [LutH]OTf (0.1 M). As illustrated in Figure S30a in the Supporting Information, the signal in the ^{15}N NMR spectrum was shifted and significantly broadened by adding [LutH]OTf. Some of the signals in No-Deuterium Proton (No-D) NMR spectra were also shifted (Figure S30b in the Supporting Information). However, the UV-vis absorption spectrum of **1a** was hardly changed even in the presence of [LutH]OTf (Figure S31 in the Supporting Information). These results suggest that the interaction between the N-H moiety in [LutH]OTf and the manganese-nitride moiety in **1a** is not strong, and the formation of a hydrogen bond rather than the protonation of the nitride moiety possibly takes place. We also conducted Stern-Volmer luminescence quenching studies of **3a** with both **1a** and [LutH]OTf (Figure S20 and Table S12 in the Supporting Information). Although the precise estimation of rate constants for the photo-induced PCET process was quite difficult due to the very high k_Q values (Table 4), the net quenching rate constants became larger than the summation of each k_Q value of **1a** and [LutH]OTf, indicating the possibility of the quenching process by PCET among **3a***, **1a**, and [LutH]OTf (see section 4.3 in the Supporting Information).

View Article Online
DOI: 10.1039/D6SC02866G

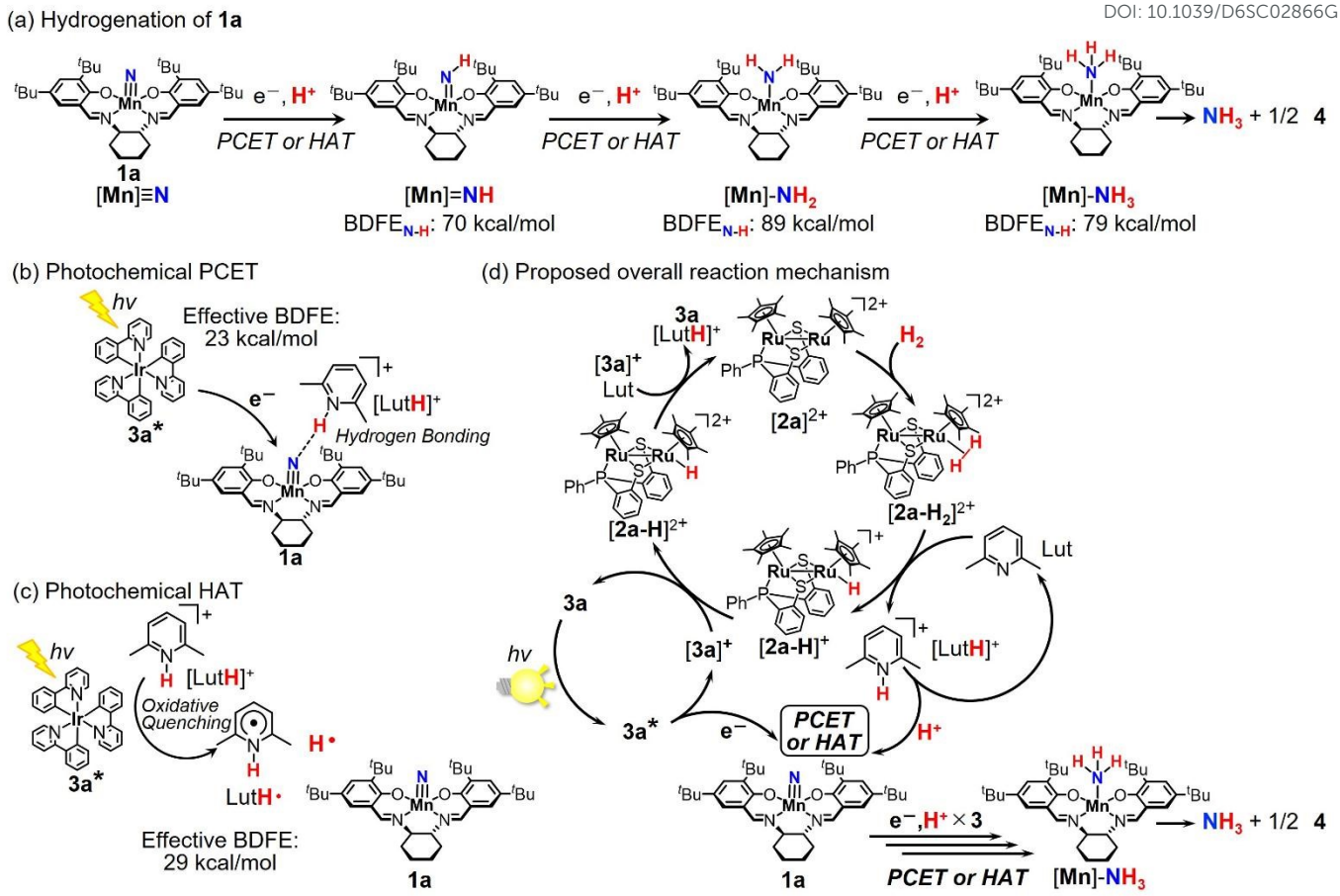

Figure 7. Photocatalytic hydrogenation of manganese nitride complexes under a dihydrogen atmosphere in the presence of **[2a-H]**OTf, **3a**, and [LutH]OTf ((a) hydrogenation steps of **1a**, (b) photochemical PCET process, (c) photochemical HAT process, (d) proposed overall reaction pathways).

Based on the abovementioned results and reported literature, the plausible reaction mechanism of the photocatalytic hydrogenation of the manganese nitride complex **1a** using the diruthenium catalyst **[2a-H]**OTf, the photosensitizer **3a**, and the proton mediator [LutH]OTf can be summarized as Figure 7d. This photocatalytic reaction is triggered by photoexcitation of **3a**, though its absorption ratio is only 11% due to the inner-filter effect of **1a**. After the photoexcitation, **3a*** is quenched mainly by **1a** (η_q = 49%) or [LutH]$^+$ (η_q = 48%). The quenching by **1a** probably includes three processes: (i) excitation energy transfer, (ii) oxidative quenching (i.e., single electron transfer from **3a*** (E_{ox}* = −2.15 V) to **1a** (E_{red} = −2.60 V)), (iii) photo-induced PCET among **3a***, **1a**, and [LutH]$^+$ (Figure 7b). Although the excitation energy transfer (path (i)) is a side reaction that suppresses photocatalysis, oxidative quenching, possibly followed by subsequent protonation (path (ii)), and photo-induced PCET (path (iii)) will hydrogenate **1a** to produce ammonia. These hydrogenation processes are exergonic because the BDFE$_{N-H}$ values of the manganese-imide, amide, and ammine complexes corresponding to **1a** are reported to be 70, 89, and 79 kcal/mol (Figure 7a),[50] respectively, which are much higher than the effective BDFE value of the combination of **3a*** and [LutH]$^+$ (23 [kcal/mol]). The photo-induced PCET might be promoted by the formation of a hydrogen bond between **1a** and [LutH]$^+$. On the other hand, the quenching by [LutH]$^+$ is probably derived from the oxidative quenching (i.e., electron transfer from **3a*** (E_{ox}* = −2.15 V) to [LutH]$^+$ (E_{red}* = −1.91 V)). The resulting LutH$^•$ radical species, of which the BDFE$_{N-H}$ value is estimated to be 29 kcal/mol, will donate a hydrogen atom to **1a** exergonically (Figure 7c). By repeating the photo-induced PCET from **3a*** and [LutH]$^+$ and/or HAT from LutH$^•$ three times, **1a** will be converted in a stepwise manner to the corresponding manganese-imide, amide, and ammine complexes, resulting in the formation of NH_3 and the dimanganese complex **4** (or its derivative caused by the interaction between **4** and [LutH]OTf). The one-electron-oxidized species of **3a** (E_{ox} = +0.27 V, **[3a]**$^+$), which is produced by the aforementioned photo-induced PCET or oxidative quenching by [LutH]$^+$, will oxidize **[2a-H]**$^+$ (E_{ox} = +0.24 V) to regenerate **3a** and produce one-electron-oxidized species of **[2a-H]**$^+$ (**[2a-H]**$^{2+}$). **[2a-H]**$^{2+}$ donates a proton and an electron to Lut and **[3a]**$^+$, respectively, to produce dicationic complex **[2a]**$^{2+}$ with a vacant site. **[2a]**$^{2+}$ reacts with a dihydrogen molecule (**[2a-H$_2$]**$^{2+}$), and **[2a-H]**$^+$ is reproduced after the deprotonation by Lut. The high acidity of **[2a-H]**$^{2+}$ and/or **[2a-H$_2$]**$^{2+}$ may have partially and directly caused the PCET process with **3a*** without the proton mediator, as demonstrated in the control experiment in Table 1. The reproduction of **[2a-H]**$^+$ proceeds

quite efficiently, leading to the procedure of photocatalytic hydrogenation of **1a** even under 0.05 atm of dihydrogen. Under the optimized conditions, photo-induced PCET to **1a** with **3a*** and $[LutH]^+$ and/or HAT from $LutH^\bullet$ to **1a** are estimated to be the plausible rate-determining steps because of the negligible effect of the increase in the concentration of **[2a]**OTf on the reaction rate and the large KIE value (>3). In contrast, under the low pressure of dihydrogen (0.2 or 0.05 atm), the rate-determining step might have switched to the reaction between $\mathbf{[2a]}^{2+}$ and dihydrogen in the catalytic cycle for dihydrogen oxidation because of the significant effect of the concentration of **[2a-H]**OTf on the reaction rate, as shown in Table 3.

Conclusions

In conclusion, we have successfully developed a visible-light-driven hydrogenation of the manganese nitride complexes to ammonia under ambient conditions by using dihydrogen as both an electron and a proton source and combining the catalytic cycle of dihydrogen oxidation with the ruthenium dinuclear complexes as catalysts and the photosensitizing cycle with the iridium complexes as photosensitizers. Our mechanistic studies proposed a plausible reaction mechanism in which photo-induced PCET and/or HAT to the manganese nitride complexes were effectively promoted by the proton mediator. Owing to the high durability of the diruthenium complex, the turnover numbers for ammonia formation based on the catalyst increased drastically (up to 150 equiv. based on the catalyst) compared with those in reported systems. Moreover, this hydrogenation proceeded photocatalytically even under 0.05 atm of dihydrogen. This feature is particularly useful to achieve the challenging target reaction, i.e., photocatalytic ammonia formation under a mixture of nitrogen and hydrogen gases, because a high partial pressure of dihydrogen often causes unexpected side reactions in the nitrogen fixation cycle; therefore, we believe that the photocatalytic hydrogenation developed in this study will function as one of the key processes for realizing catalytic ammonia production from dinitrogen and dihydrogen under ambient reaction conditions, and further studies on developing such photocatalytic system are currently underway.

Author contributions

Y.N. conceived and designed this project. Q.W. mainly conducted the experimental work. Y.T. mainly analyzed crystal structures by using X-ray diffraction measurements. Y.Y. mainly analyzed experimental data and prepared the first draft of the manuscript. All authors discussed the results and drafted the manuscript.

Conflicts of interest

There are no conflicts to declare.

Data availability

The data supporting this article have been included as part of the Supplementary Information. CCDC 2413808 (for **1c**) and 2413811 (for **4**) contain the supplementary crystallographic data for this paper.

Acknowledgements

We acknowledge the Grants-in-Aid for Scientific Research (Nos. 20H05671, 24H00049, 24H01834, 24K21778, JP23H03832, JP23H03830, and 24K08441) from JSPS and MEXT. This paper is based on results obtained from a project, JPNP 21020, commissioned by the New Energy and Industrial Technology Development Organization (NEDO).

References

1 H. Liu, *Chin. J. Catal.*, 2014, **35**, 1619-1640.
2 X. Wang, W. Fan, J. Chen, G. Feng, X. Zhang, *Fuel*, 2022, **329**, 125496.
3 J. Guo, P. Chen, *Chem*, 2017, **3**, 709-712.
4 K. Mazloomi, C. Gomes, *Renew. Sustain. Energy Rev.*, 2012, **16**, 3024-3033.
5 C. Smith, A. K. Hill, L. Torrente-Murciano, *Energy Environ. Sci.*, 2020, **13**, 331-344.
6 V. N. Sagel, K. H. R. Rouwenhorst, J. A. Faria, *Renew. Sustain. Energy Rev.*, 2022, **161**, 112381.
7 S. Zhang, Y. Zhao, R. Shi, G. I. N. Waterhouse, T. Zhang, *EnergyChem*, 2019, **1**, 100013.
8 S. Lin, X. Zhang, L. Chen, Q. Zhang, L. Ma, J. Liu, *Green Chem.*, 2022, **24**, 9003-9026.
9 Y. Shi, Z. Zhao, D. Yang, J. Tan, X. Xin, Y. Liu, Z. Jiang, *Chem. Soc. Rev.*, 2023, **52**, 6938-6956.
10 S. Joseph Sekhar, A. Said Ahmed Al-Shahri, G. Glivin, T. H. T. Le, T. Mathimani, *Fuel*, 2024, **358**, 130307.
11 G. Jia, R. H. Morris, C. T. Schweitzer, *Inorg. Chem.*, 2002, **30**, 593-594.
12 Y. Nishibayashi, S. Iwai, M. Hidai, *Science*, 1998, **279**, 540-542.
13 Y. Nishibayashi, S. Takemoto, S. Iwai, M. Hidai, *Inorg. Chem.*, 2000, **39**, 5946-5957.
14 Y. Nishibayashi, I. Wakiji, K. Hirata, M. R. DuBois, M. Hidai, *Inorg. Chem.*, 2001, **40**, 578-580.
15 J. A. Pool, E. Lobkovsky, P. J. Chirik, *Nature*, 2004, **427**, 527-530.
16 J. A. Pool, W. H. Bernskoetter, P. J. Chirik, *J. Am. Chem. Soc.*, 2004, **126**, 14326-14327.
17 W. H. Bernskoetter, E. Lobkovsky, P. J. Chirik, *J. Am. Chem. Soc.*, 2005, **127**, 14051-14061.
18 D. Pun, C. A. Bradley, E. Lobkovsky, I. Keresztes, P. J. Chirik, *J. Am. Chem. Soc.*, 2008, **130**, 14046-14047.
19 M. Reiners, D. Baabe, K. Munster, M. K. Zaretzke, M. Freytag, P. G. Jones, Y. Coppel, S. Bontemps, I. D. Rosal, L. Maron, M. D. Walter, *Nat. Chem.*, 2020, **12**, 740-746.
20 X. Xin, I. Douair, Y. Zhao, S. Wang, L. Maron, C. Zhu, *Natl. Sci. Rev.*, 2023, **10**, nwac144.
21 C. E. Laplaza, C. C. Cummins, *Science*, 1995, **268**, 861-863.
22 T. J. Hebden, R. R. Schrock, M. K. Takase, P. Muller, *Chem. Commun.*, 2012, **48**, 1851-1853.
23 I. Klopsch, M. Finger, C. Wurtele, B. Milde, D. B. Werz, S. Schneider, *J. Am. Chem. Soc.*, 2014, **136**, 6881-6883.
24 C. Rebreyend, B. de Bruin, *Angew. Chem. Int. Ed.*, 2015, **54**, 42-44.

25 B. M. Lindley, R. S. van Alten, M. Finger, F. Schendzielorz, C. Wurtele, A. J. M. Miller, I. Siewert, S. Schneider, *J. Am. Chem. Soc.*, 2018, **140**, 7922-7935.
26 F. Hasanayn, P. L. Holland, A. S. Goldman, A. J. M. Miller, *J. Am. Chem. Soc.*, 2023, **145**, 4326-4342.
27 Y. Ashida, K. Arashiba, K. Nakajima, Y. Nishibayashi, *Nature*, 2019, **568**, 536-540.
28 Y. Ashida, T. Mizushima, K. Arashiba, A. Egi, H. Tanaka, K. Yoshizawa, Y. Nishibayashi, *Nat. Synth.*, 2023, **2**, 635-644.
29 Y. Ashida, Y. Onozuka, K. Arashiba, A. Konomi, H. Tanaka, S. Kuriyama, Y. Yamazaki, K. Yoshizawa, Y. Nishibayashi, *Nat. Commun.*, 2022, **13**, 7263.
30 Y. Yamazaki, Y. Endo, Y. Nishibayashi, *Nat. Commun.*, 2025, **16**, 4540.
31 Y. Tanabe, Y. Nishibayashi, *Chem. Soc. Rev.*, 2021, **50**, 5201-5242.
32 Y. Tanabe, Y. Nishibayashi, *Coord. Chem. Rev.*, 2022, **472**, 214783.
33 Y. Tanabe, Y. Nishibayashi, *Angew. Chem. Int. Ed.*, 2024, **63**, e202406404.
34 B. Peigne, G. Aullon, *Acta Crystallogr. B Struct. Sci. Cryst. Eng. Mater.*, 2015, **71**, 369-386.
35 D. V. Yandulov, R. R. Schrock, *Science*, 2003, **301**, 76-78.
36 J. S. Anderson, J. Rittle, J. C. Peters, *Nature*, 2013, **501**, 84-87.
37 M. J. Chalkley, M. W. Drover, J. C. Peters, *Chem. Rev.*, 2020, **120**, 5582-5636.
38 Q. J. Bruch, G. P. Connor, N. D. McMillion, A. S. Goldman, F. Hasanayn, P. L. Holland, A. J. M. Miller, *ACS Catal.*, 2020, **10**, 10826-10846.
39 Q. J. Bruch, S. Malakar, A. S. Goldman, A. J. M. Miller, *Inorg. Chem.*, 2022, **61**, 2307-2318.
40 L. Merakeb, S. Bennaamane, J. De Freitas, E. Clot, N. Mezailles, M. Robert, *Angew. Chem. Int. Ed.*, 2022, **61**, e202209899.
41 H. P. Jia, E. A. Quadrelli, *Chem. Soc. Rev.*, 2014, **43**, 547-564.
42 S. J. K. Forrest, B. Schluschass, E. Y. Yuzik-Klimova, S. Schneider, *Chem. Rev.*, 2021, **121**, 6522-6587.
43 K. C. Macleod, P. L. Holland, *Nat. Chem.*, 2013, **5**, 559-565.
44 S. Kim, H. Zhong, Y. Park, F. Loose, P. J. Chirik, *J. Am. Chem. Soc.*, 2020, **142**, 9518-9524.
45 C. M. Johansen, E. A. Boyd, J. C. Peters, *Sci. Adv.*, 2022, **8**, eade3510.
46 C. M. Johansen, E. Benazzi, J. C. Peters, *Proc. Natl. Acad. Sci. U. S. A.*, 2025, **122**, e2502484122.
47 M. H. Huynh, T. J. Meyer, *Chem. Rev.*, 2007, **107**, 5004-5064.
48 M. T. Koper, *Phys. Chem. Chem. Phys.*, 2013, **15**, 1399-1407.
49 P. Garrido-Barros, J. Derosa, M. J. Chalkley, J. C. Peters, *Nature*, 2022, **609**, 71-76.
50 G. B. Panetti, J. Kim, M. S. Myong, M. J. Bird, G. D. Scholes, P. J. Chirik, *J. Am. Chem. Soc.*, 2024, **146**, 27610-27621.
51 S. Kim, Y. Park, J. Kim, T. P. Pabst, P. J. Chirik, *Nat. Synth.*, 2022, **1**, 297-303.
52 Y. Park, S. Kim, L. Tian, H. Zhong, G. D. Scholes, P. J. Chirik, *Nat. Chem.*, 2021, **13**, 969-976.
53 J. Kim, G. B. Panetti, N. Kaul, S. Kim, P. J. Chirik, *J. Am. Chem. Soc.*, 2025, **147**, 8215-8226.
54 Y. Park, L. Tian, S. Kim, T. P. Pabst, J. Kim, G. D. Scholes, P. J. Chirik, *JACS Au*, 2022, **2**, 407-418.
55 M. Yuki, K. Sakata, Y. Hirao, N. Nonoyama, K. Nakajima, Y. Nishibayashi, *J. Am. Chem. Soc.*, 2015, **137**, 4173-4182.
56 M. Yuki, K. Sakata, K. Nakajima, S. Kikuchi, S. Sekine, H. Kawai, Y. Nishibayashi, *Organometallics*, 2017, **36**, 4499-4506.
57 M. Yuki, K. Sakata, S. Kikuchi, H. Kawai, T. Takahashi, M. Ando, K. Nakajima, Y. Nishibayashi, *Chem. Eur. J.*, 2017, **23**, 1007-1012.
58 C. G. Hatchard, C. A. Parker, *Proc. R. Soc. A.*, 1956, **235**, 518-536.
59 J. D. Steen, D. R. Duijnstee, W. R. Browne, *Surf. Sci. Rep.*, 2023, **78**, 100596.
60 D. Wang, F. Loose, P. J. Chirik, R. R. Knowles, *J. Am. Chem. Soc.*, 2019, **141**, 4795-4799.
61 G. C. Dailey, C. P. Horwitz, C. A. Lisek, *Inorg. Chem.*, 2002, **31**, 5325-5330.
62 F. K. Larsen, E. J. McInnes, H. El Mkami, J. Overgaard, S. Piligkos, G. Rajaraman, E. Rentschler, A. A. Smith, G. M. Smith, V. Boote, M. Jennings, G. A. Timco, R. E. Winpenny, *Angew. Chem. Int. Ed.*, 2003, **42**, 101-105.
63 A. K. Kar, A. Acharya, G. C. Pradhan, A. C. Dash, *J. Chem. Sci.*, 2014, **126**, 547-559.
64 G. H. Allen, R. P. White, D. P. Rillema, T. J. Meyer, *J. Am. Chem Soc.*, 1984, **106**, 2613-2620.

View Article Online
DOI: 10.1039/D6SC02866G

View Article Online
DOI: 10.1039/D6SC02866G

The data supporting this article have been included as part of the Supplementary Information.

CCDC (2413808 and 2413811) contain the supplementary crystallographic data for this paper.